ACADEMIC PRESS

Available online at www.sciencedirect.com

SCIENCE DIRECT®

Journal of Sound and Vibration 263 (2003) 175–204

JOURNAL OF SOUND AND VIBRATION

www.elsevier.com/locate/jsvi

Dynamic stability of weakly damped oscillators with elastic impacts and wear

J. Knudsen[a,b,*], A.R. Massih[a,c]

[a] *Division of Materials Science, Malmö University, SE 205 06 Malmö, Sweden*
[b] *Luleå University of Technology, SE 971 87 Luleå, Sweden*
[c] *Quantum Technologies AB, Uppsala Science Park, SE 751 83 Uppsala, Sweden*

Received 12 November 2001; accepted 22 April 2002

Abstract

The dynamics of non-linear oscillators comprising of a single-degree-of-freedom system and beams with elastic two-sided amplitude constraints subject to harmonic loads is analyzed. The beams are clamped at one end, and constrained against unilateral contact sites near the other end. The structures are modelled by a Bernoulli-type beam supported by springs using the finite element method. Rayleigh damping is assumed. Symmetric and elastic double-impact motions, both harmonic and sub-harmonic, are studied by way of a Poincaré mapping that relates the states at subsequent impacts. Stability and bifurcation analyses are performed for these motions, and domains of instability are delineated. Impact work rate, which is the rate of energy dissipation to the impacting surfaces, is evaluated and discussed. In addition, an experiment conducted by Moon and Shaw on the vibration of a cantilevered beam with one-sided amplitude constraining stop is modelled. Bifurcation observed in the experiment could be captured.

1. Introduction

Oscillating mechanical systems confined within barriers exhibit highly non-linear behaviour due to impacting. These oscillators are frequently encountered in many industrial equipment such as steam generator tubes and fuel rods in nuclear power plants [1], impacting hammers [2], hopping

*Corresponding author. Division of Materials Science, Malmö University, SE 205 06 Malmö, Sweden. Fax: 40665-7135.

E-mail address: tsjakn@ts.mah.se (J. Knudsen).

0022-460X/03/$ - see front matter
PII: S0022-460X(02)01104-5

robots [3] and gear transmissions [4], to name a few. Commonly, impacting is associated with increase wear of the components of the oscillator, which is related to the dynamical behaviour of the system. Hence, the study of vibro-impact dynamics is important for understanding and analyzing the wear of components that are under such motions. The simplest model for vibro-impacting system is a spring–mass system with amplitude constraint. A single-degree-of-freedom oscillator (s.d.o.f.) with one-sided elastic constraint has been studied by Shaw and Holmes [5]. They found harmonic, sub-harmonic, and chaotic motions and analyzed the bifurcations leading to them. Shaw [6] considered the dynamics of an s.d.o.f. with two-sided rigid constraints. The vibro-impact dynamics of multi-d.o.f. systems has been the topic of several investigations. Aidanpää and Gupta [7] analyzed the one-sided impact motion of a two-d.o.f. impact vibrator. They studied the influence of system parameters and compared the dynamic response behaviour of a two-d.o.f. with that of an s.d.o.f. Pun et al. [8] investigated the dynamics of a multi-d.o.f. impact vibrator subject to harmonic loading bound by rigid walls.

The impetus for the present study stems from applications in nuclear reactor components such as fuel rods and steam generator tubes, which are subject to flow-induced vibrations. Steam generator tubes are designed to have gaps at support points to allow for thermal expansion and in nuclear fuel systems gaps may develop during service due to relaxation of support springs and creep down of cladding tubes. In these systems, the rods vibrate in many modes and are subjected to random, turbulent forces. The wear of these tubes is a major technical issue in the industry [1,9]. In previous studies, the authors have analyzed the vibro-impact dynamics of beams subject to harmonic loads [10] and random loads [11]. The results of these analyses were compared with measurements of contact forces and displacements made on a loosely supported rod in experiments. To characterize the system dynamics an s.d.o.f. system with two-sided elastic constraints subject to both harmonic and random loads [10,11] was evaluated. For the sake of comparison, a two-dimensional beam with two-diametrically opposed identical supports was also modelled using the finite element method. Both systems exhibit aperiodic as well as periodic solutions when subjected to harmonic forces. But when the systems were subjected to random forces no periodic solutions were found.

In this paper, the details of the dynamic stability of damped impact oscillators with elastic constraints subject to harmonic loads are studied. A beam oscillator and its equivalent s.d.o.f. systems are considered. The beam oscillator geometry and configuration are the same as that studied in the authors' earlier papers [10,11] where the results of computations were compared with measurements. Furthermore, the energy dissipated under impacting is evaluated which is an important measure of wear for such systems. An attempt was also made to numerically simulate, using the given method, an experiment on the vibration of a cantilevered beam with non-linear boundary condition made by Moon and Shaw [12].

The organization of this paper is as follows. A forced simple damped harmonic oscillator (SDHO) with two-sided elastic constraints is considered in Section 2 where its dynamics is described and the method utilized for stability analysis is delineated. Section 3 treats the dynamics of vibrating beams comprising of a beam with fuel rod dimensions and the Moon and Shaw cantilever beam used in their experiment. In Section 4, the common methods used for the analysis of the beams and the s.d.o.f. system are detailed. The work rate and a method of finding the periodic orbits and the bifurcation points of the system are also studied in

Section 4. The results of the computations are presented in Section 5 for the considered mechanical systems.

2. Simple damped harmonic oscillator

2.1. Oscillator

A s.d.o.f. system consisting of a SDHO with symmetric elastic constraints is considered here. The oscillator consists of a point mass suspended horizontally by a linear spring and a linear damper. An applied force brings the mass into contact with one of the two elastic contact sites, which are linear springs as shown in Fig. 1.

The dynamics for this system is described by the following second order differential equation [10,11]:

$$x_{,\tau\tau} + 2\zeta x_{,\tau} + h(x) = \beta\cos(\omega\tau), \tag{1}$$

where $h(x) = x$ for $|x| < 1$ and $h(x) = w^2x - (w^2 - 1)\,\mathrm{sgn}(x)$ for $|x| \geqslant 1$. Further, $w^2 = (k_1 + k_2)/k_1$, $x = X/X_0$, $\tau = \omega_0 t$, $(\,)_{,\tau} = \partial(\,)/\partial\tau$, $\omega_0^2 = k_1/m$, $2\zeta = c/(m\omega_0)$, $\omega = \Omega/\omega_0$ and $\beta = A/(m\omega_0^2 X_0)$. Fig. 1 defines the remaining variables.

Hence, the dynamical system is characterized by the following variable quadruple $(\omega, \beta, \zeta, w^2)$, i.e., the forcing frequency, the forcing amplitude, the damping ratio and the stiffness ratio, respectively. Moreover, the state of the system is determined by the vector (x, v, τ). The analytic solution of Eq. (1) is presented in Appendix A.

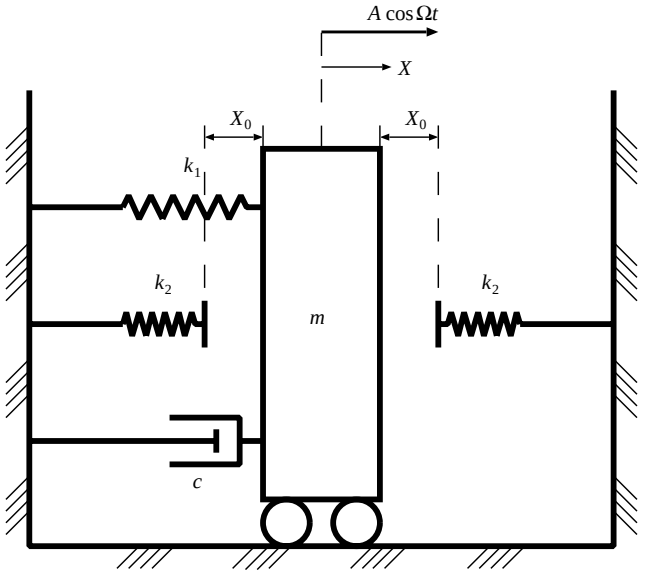

Fig. 1. A two-sided simple damped harmonic oscillator with elastic supports.

2.2. Dynamics

Next, rewrite the second order equation (1) in the form of a system of first order equations:

$$x_{,\tau} = v,$$

$$v_{,\tau} = -2\zeta v - h(x) + \beta\cos(\omega\tau),$$

$$\tau_{,\tau} = 1. \tag{2}$$

Hence, the state of the system is determined by (x, v, τ).

The three-dimensional vector field defined in Eq. (2) is periodic in τ with period $2\pi/\omega$. The vector field dimension is reduced by defining a one-sided Poincaré section at the place of structural contact, i.e., at $|x| = 1$, which gives two possibilities:

$$\Sigma^{+} = \{(x, v, \tau)|x = +1, v > 0\}, \quad \Sigma^{-} = \{(x, v, \tau)|x = -1, v < 0\}. \tag{3}$$

Next a Poincaré return map $\mathbf{P}$ is defined as a mapping of points in Σ into themselves:

$$\mathbf{P} = \Sigma \to \Sigma \quad \text{or} \quad (\tau_N, v_N) = \mathbf{P}(\tau_0, v_0), \tag{4}$$

where Σ denotes either of the two sections defined in (3), which are selected depending on the sign of the initial velocity v_0, and N is an even integer number. It is assumed that the iteration (in forward time) begins with a non-linear contact phase (i.e., when a contact spring is compressed) and then followed by a linear free-flight phase.

2.3. Periodic orbits

Periodic motion of the SDHO is studied by using the Poincaré map $\mathbf{P}$. A motion that repeats itself after k encounters with the Poincaré section must fulfill the following condition:

$$\left(\bar{\tau} + \frac{2\pi n}{\omega}, \bar{v}\right) = P^{k}(\bar{\tau}, \bar{v}), \tag{5}$$

where P^k denotes the kth iterated map and n is the order of sub-harmonic. The point $(\bar{\tau}, \bar{v})$ is called periodic in P. Note that relation (5) holds for both symmetric ($2k$ impact motion) and non-symmetric periodic motion after impacts at $x = \pm 1$.

The stability of a periodic motion can be found by evaluating the eigenvalues of the Jacobian matrix of the return map at $(\bar{\tau}, \bar{v})$. In Shaw's fashion [6], the Jacobian is written in the form

$$\mathbf{J} = \left[\frac{\partial(\tau_{\mathrm{N}}, v_{\mathrm{N}})}{\partial(\tau_{\mathrm{N}-1}, v_{\mathrm{N}-1})}\right] \cdots \left[\frac{\partial(\tau_2, v_2)}{\partial(\tau_1, v_1)}\right]\left[\frac{\partial(\tau_1, v_1)}{\partial(\tau_0, v_0)}\right], \tag{6}$$

where the chain rule was utilized. The components of the (4×4) matrices are listed in Appendix B. Note that, due to the transcendental nature of the solution (Eq. (A.1), Appendix A), P is not known in closed form and hence in order to evaluate it one has to resort to numerical methods.

2.4. Method of computation

The method of computation of trajectories and intersections with the Poincaré sections is as follows: Evaluate Eq. (A.1) in Appendix A for the time τ_{i+1} at the next structural discontinuity,

i.e., solve

$$|x(\tau_{i+1};\tau_i,v_i)|-1=0,\quad \tau_{i+1}>\mathrm{sgn}(\tau)\tau_i, \tag{7}$$

where (τ_i, v_i) denotes the initial state.

Given the triple (τ_{i+1},τ_i,v_i), the variables $v_{i+1}=x_{,\tau}|_{\tau=\tau_{i+1}}$ and $a_{i+1}=v_{,\tau}|_{\tau=\tau_{i+1}}$ are explicitly found through differentiations of Eq. (A.1) with respect to τ:

$$\begin{aligned} v_{i+1}=&\,\mathrm{e}^{-\zeta(\tau_{i+1}-\tau_i)}\{(-\zeta A_i+\Omega_i B_i)\cos[\Omega_i(\tau_{i+1}-\tau_i)]-(\Omega_i A_i+\zeta B_i)\sin[\Omega_i(\tau_{i+1}-\tau_i)]\}\\ &-\gamma_i\omega\sin(\omega\tau_{i+1})+\delta_i\omega\cos(\omega\tau_{i+1}), \end{aligned} \tag{8}$$

$$\begin{aligned} a_{i+1}=&\,\mathrm{e}^{-\zeta(\tau_{i+1}-\tau_i)}\{(\zeta^2A_i-2\zeta\Omega_iB_i-\Omega_i^2A_i)\cos[\Omega_i(\tau_{i+1}-\tau_i)]\\ &+(\zeta^2B_i+2\zeta\Omega_iA_i-\Omega_i^2B_i)\sin[\Omega_i(\tau_{i+1}-\tau_i)]\}\\ &-\gamma_i\omega^2\cos(\omega\tau_{i+1})-\delta_i\omega^2\sin(\omega\tau_{i+1}), \end{aligned} \tag{9}$$

where A_i, B_i, Ω_i, γ_i and δ_i are defined in relations (A.2) in Appendix A.

The root of Eq. (A.1) in Appendix A is calculated by first bracketing the root and then applying a Newton–Raphson (NR) iteration scheme. The NR iteration scheme that is utilized is very robust and fast, once the root is bracketed. However, bracketing the correct root is a non-trivial task, since the duration of contact and free-flight phases can vary greatly. The scheme of the computation is outlined in Box 1, where square brackets [] and][denote closed and open intervals, respectively.

The algorithm outlined in Box 1 has been found to be very robust and efficient, i.e., for the type of problems considered here, it gives rapid convergence. However, it should be mentioned that the algorithm fails for specific situations: (i) when no contacts occur and (ii) when the difference

Box 1
SDHO computational scheme.

(1) Initial interval guess $[\tau^1,\tau^2]$, where $\tau^1>\mathrm{sgn}(\tau)\tau_i$ and $\tau^2=\tau_i+\mathrm{sgn}(\tau)2\pi n/\omega$.
(2) Divide the interval into $i_n n_{div}$ sub-intervals.
(3) Loop through the sub-intervals to find sign change of $|x|-1$. If no sign change is found, set $i_n := i_n+1$ and go to step 2, else set $[\tau^{b1},\tau^{b2}]$ to bracket the change of sign.
(4) Run NR iteration to find root $\tau^r\in[\tau^{b1},\tau^{b2}]$.
(5) Verify the root τ^r in
- contact phase

$$x(\tau;\tau_i,v_i)\,\mathrm{sgn}(\tau)\,\mathrm{sgn}(v_i)\geqslant 1\quad \text{for } \tau\in]\tau_i,\tau^r[;$$

- free-flight phase

$$|x(\tau;\tau_i,v_i)|<1\quad \text{for } \tau\in]\tau_i,\tau^r[.$$

If the root is not valid, set $i_n := i_n+1$ and if $(i_n>8)$ set $\tau^1:=(\tau_i+\tau^1)/2$ go to step 2.
(6) Set $\tau_{i+1}=\tau^r$ and $\tau^1=\tau^{b2}$ and proceed with next phase.

between the duration of contact and free-flight phase is very large. In both situations, the algorithm fails due to the inability to bracket a root.

3. Vibrating beams

3.1. Beam oscillators

Three different types of impact oscillators involving beams are studied in this paper: (i) a beam representation of an SDHO, Section 3.1.1, (ii) an experiment by Moon and Shaw [12], Section 3.1.2 and (iii) vibration of a nuclear fuel rod [10,13,14], Section 3.1.3. The main purpose of the first two oscillators is to gain understanding for details of the dynamics of the system and also to validate the numerical methods utilized. The third oscillator illustrates an application of the methods to an engineering structure.

The structures are considered to be Bernoulli beams with Rayleigh damping [15]. The beam is discretized in space with finite elements with cubic interpolation functions and in time using Newmark's integration method [16]. The program uses a node-to-node contact algorithm; hence, each contact sites is connected to a specific node. Each contact site can be given individual force–displacement relationship in normal, tangential, and axial directions. Stick–slip motion along the curved surface of the beam is allowed. The contact force vector $\mathbf{p}$ is resolved into $\mathbf{p} = (p_n, p_c, p_a)$, where indices n, c and a denote normal, circumferential and axial directions, respectively. Correspondingly, the gap vector is decomposed as $\mathbf{g} = (g_n, g_c, 0)$. Classical contact laws (Signorini plus Coulomb) are assumed, see e.g., Refs. [10,17]. Since the present work deals with planar beams only, the circumferential components are set equal to zero. Furthermore, because the deflections are small, set $p_a = 0$. Hence, friction force does not enter the calculations here. The model has been used to analyze beam vibrations in our earlier works [10,11,13,14] with and without friction.

3.1.1. Beam representation of the SDHO

The SDHO described in Section 2 is revisited. However, this time the point mass is considered as a cylindrical beam of unit length and radius with a high bending stiffness. Damping is introduced through a potential damper according to Fig. 1.

The beam is modelled with two finite elements of length 0.5, whose rotational d.o.f. have been locked. Hence one has a system consisting of three d.o.f. This system is excited with a harmonic force at a point halfway along the beam, where the contact sites are also placed.

The purpose of this fictitious beam is to facilitate the verification of the numerical methods, to be described later in this section, used to compute fixed points and local bifurcations of vibrating beams through direct comparison with the SDHO.

3.1.2. Moon and Shaw experiment

Consider an experiment conducted by Moon and Shaw [12], where a cantilever beam was excited by prescribing the displacement at the fixed end. The motion of the free end was constrained by an aluminium stop, limiting the amplitude of the free end in one direction as shown on the left-hand side of Fig. 2.

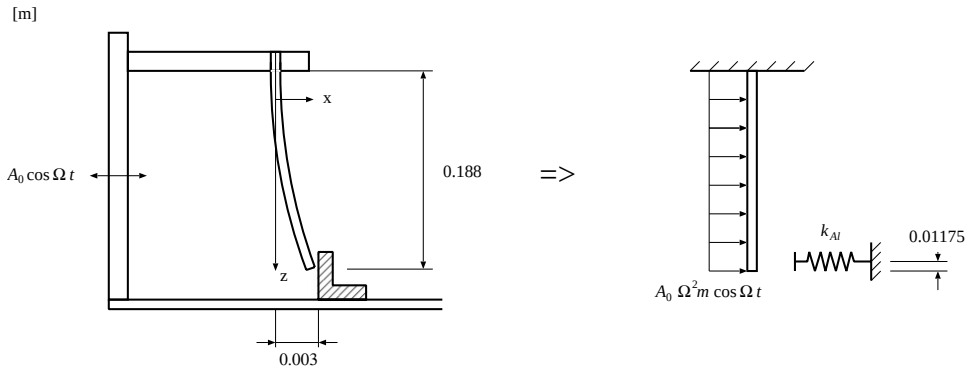

Fig. 2. Moon and Shaw experiment [12].

Since our code is currently not equipped to handle prescribed displacement boundary conditions, the displacement load is translated to a distributed load along the beam as indicated on the right side of Fig. 2.

The reason for considering this beam oscillator here is not only to show that the method can be used to evaluate such an experiment, but also to verify that the applied numerical method is capable of producing features observed in the real world. However, in order to evaluate the experiment accurately it is necessary to pay more attention to details of damping and the boundary conditions. This will be discussed more in the computation and conclusion sections of this paper (Sections 5 and 6).

3.1.3. *Fuel rod oscillator*

Consider a long slender beam supported at one end by a pair of stiff springs, namely a torsion spring with stiffness k_{rot} suppressing rotation and a lateral spring with stiffness k_{tra} suppressing translation. Also, the beam is constrained by symmetric contact sites situated near the other end, see Fig. 3. The beam is modelled with finite elements (FE) and the contact sites with linear elastic springs. The beam is excited with a harmonic force applied in the same plane as the contact sites. The case considered here was the object of an experiment, performed on a portion of nuclear fuel rod, which was analyzed in the authors' previous papers [10,11].

3.2. *Dynamics*

The dynamics of the FE system of the type described in the previous section (Section 3.1), in non-dimensional form, can be written as a system of first order differential equations:

$$\mathbf{x}_{,\tau} = \mathbf{v},$$

$$\mathbf{v}_{,\tau} = \mathbf{M}^{-1}[\mathbf{f}_a + \mathbf{f}_c - \mathbf{C}\mathbf{v} - \mathbf{K}\mathbf{x}],$$

$$\tau_{,\tau} = 1, \tag{10}$$

where $\mathbf{M}$, $\mathbf{C}$ and $\mathbf{K}$ are the consistent mass, damping and stiffness matrices, respectively, $\mathbf{x}$ and $\mathbf{v}$ are the displacement and velocity vectors, respectively, $\mathbf{f}_a$ is the applied force and $\mathbf{f}_c$ is the contact

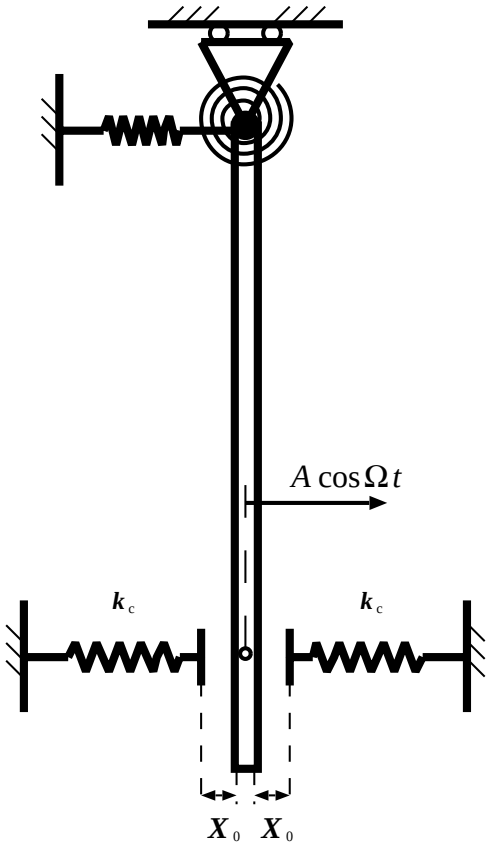

Fig. 3. A two-sided beam impact oscillator.

force. Consequently, the state vector for the system is defined by $(\mathbf{x}, \mathbf{v}, \tau)$. The vector field defined in (10) has dimension $(2n_{d.o.f.} + 1)$, where $n_{d.o.f.}$ is the number of d.o.f. of the system. For a harmonic load with forcing frequency Ω, the field is periodic in τ with period $2\pi/\omega$, where $\omega = \Omega/\omega_0$ is the non-dimensional forcing frequency and ω_0 is the fundamental eigenfrequency of the system. Further, $\mathbf{X} = \mathbf{x}X_0$ and $\tau = \omega_0 t$, where $\mathbf{X}$ denotes the dimensional displacement vector, X_0 is the initial gap and t is the time.

Like the SDHO case, a one-sided Poincaré section is defined. Since a node-to-node contact algorithm is being used, the node x_c, where structural contact will occur, is identified and the section defined by

$$\Sigma = \{(\mathbf{x}, \mathbf{v}, \tau) \,|\, x_c = +1, v_c > 0\} \tag{11}$$

and the corresponding return map $\mathbf{P}$ by

$$\mathbf{P} = \Sigma \to \Sigma \quad \text{or} \quad (\hat{\tau}, \hat{\mathbf{x}}^r, \hat{\mathbf{v}}) = \mathbf{P}(\tau, \mathbf{x}^r, \mathbf{v}), \tag{12}$$

where $\mathbf{x}^r$ is the reduced displacement vector, i.e., we exclude the contact node $x_c = +1$, and use the hat symbol $\hat{}$ to denote the quantities at the subsequent structural contact.

3.3. Periodic orbits

For a beam oscillator, a fixed point of the return map **P** in (12), i.e., harmonic motion of the system in Eq. (10), satisfies the following condition:

$$\left(\bar{\tau} + \frac{2\pi n}{\omega}, \bar{\mathbf{x}}^r, \bar{\mathbf{v}}\right) = \mathbf{P}^k(\bar{\tau}, \bar{\mathbf{x}}^r, \bar{\mathbf{v}}), \tag{13}$$

where n denotes the sub-harmonic of the k iterated map.

The local stability of the periodic point is given by the eigenvalues of the Jacobian matrix evaluated at the periodic point. The Jacobian is calculated with a forward difference approximation and the eigenvalues thereof are computed using a Hessenberg reduction of the Jacobian and then applying a QR algorithm [18]. The QR algorithm is an iterative procedure which converges to a form where the eigenvalues are isolated on the diagonal or are eigenvalues of a (2×2) sub-matrix. It is called QR because in each iteration the **QR** decomposition of a matrix $\mathbf{A}_i = \mathbf{QR}$ is computed, where $\mathbf{QQ}^{\mathrm{T}} = 1$ and **R** is an upper triangular matrix.

3.4. Method of computation

The procedure for computing one or more iterates of the Poincaré return map, given by Eq. (12), is to start from the initial state $(\bar{\tau}, \bar{\mathbf{x}}^r, \bar{\mathbf{v}})$ with $x_c = +1$, then step forward in time until $\hat{x}_c(\hat{\tau}) = +1$ for $\hat{\tau} > \bar{\tau}$, where $\hat{\tau}$ denotes the time at the subsequent impact at the same contact site.

The efficiency of following vibro-impact dynamics in the time domain using an FE code is well documented, where the pseudo-force formulation with an implicit Newmark integration scheme enables the use of a relatively large time step [16]. However, the incremental formulation can only approximate $\hat{\tau}$ in the closed interval $[\tau_i, \tau_i + \Delta\tau]$ (subscript i is used to number the increments).

One should remark that an error in the computation of the final state $(\hat{\tau}, \hat{\mathbf{x}}^r, \hat{\mathbf{v}})$ will propagate into the evaluation of the Jacobian. Therefore, it is necessary to select a sufficiently small time step to obtain the desired accuracy of the Jacobian. However, it is not feasible to use the "small" time step for the entire time integration. Therefore either an adaptive technique or an interpolation scheme was used in the analysis. The simple adaptive "micro-shooting" algorithm, outlined in Box 2, has been found to be very robust and reliable; robust in the sense that it will not diverge and is reliable, meaning that it estimates the impact time with sufficient accuracy for the problem under consideration.

The major drawback of the algorithm, outlined in Box 2, is its efficiency. Compared to an interpolation scheme this algorithm needs far more operations and it is necessary to make sure that the time increment used to improve the impact time estimate stays above the machine accuracy. Here, this is implemented using the FORTRAN90 "EPSILON" function, e.g., Ref. [19]. The drawbacks are, however, considered to be minor, due to the simplicity and reliability of the algorithm. Furthermore, the extra operations used are small compared to the total number of steps needed in the time integration and the Newton iteration. One should mention that a scheme using linear interpolation was implemented and later discarded, since it failed to produce the necessary accuracy for the calculation of the Jacobian, which leads to slow convergence, if any, and frequently gave incorrect eigenvalues.

Box 2
Micro-shooting algorithm.

(1) Proceed time stepping until an impact is detected. Impacts are identified by $p_n^i = 0$ and $p_n^{i+1} > 0$, where i denotes the increments.
(2) If the number of impacts equals the number of map iterations k and $x_c^{i+1} - 1 > \texttt{tol} > 0$, where predefined `tol` is a tolerance, proceed to step 3, otherwise report the state and end.
(3) Increase m with one, where m is the number of iterations needed to find the impact time.
(4) If this is the first time ($m = 1$), set

$$\Delta\tau_0 = \Delta\tau,$$

$$\tilde{\tau} = \tau^{i+1} - \Delta\tau/2$$

and go to step 6. $\tilde{\tau}$ is an estimate of the impact time.
(5) Update the impact time estimate according to:
If $\tau^{i+1} > \tilde{\tau}$

$$\tilde{\tau} = \tilde{\tau} + \Delta\tau_0/2^m$$

otherwise

$$\tilde{\tau} = \tilde{\tau} - \Delta\tau_0/2^m$$

(6) Re-instate the state for $i - 1$, set $\Delta\tau = (\tilde{\tau} - \tau^{i-1})/2$ and reduce the impact number (counter) by 1, then re-enter the time stepping at 1.

4. Common methods

The same formalism has intentionally been used for the oscillators described in Sections 2 and 3. This enables one to make use of the same methods to perform separate desirable computations. These methods are outlined below.

4.1. Impact work-rate

Impact wear damage is quantified with the impact work-rate [20] parameter, which essentially is a measure of available power to produce damage at the supports. Following Ref. [10], the incremental normal work-rate is defined to be $\mathrm{d}U_n = p\,\mathrm{d}s$, where p and s denote contact force acting on the support and its displacement, respectively. Returning to the global variables, defined in Sections 2 and 3, write

$$\begin{aligned}\mathrm{d}U_n &= k_2(|X| - X_0)\,\mathrm{d}(|X| - X_0)\\ &= k_2(|X| - X_0)|\dot{X}|\,\mathrm{d}t,\end{aligned} \tag{14}$$

which is rewritten in non-dimensional form as

$$\mathrm{d}u = [|x| - 1]|v|\,\mathrm{d}\tau, \tag{15}$$

where $\mathrm{d}u = \mathrm{d}U_n/(k_2 X_0^2)$. Note that impacts occurring at $x = \pm 1$ are accounted for by taking the absolute value of x. The time-averaged work-rate is consequently

$$\langle \dot{U} \rangle = \frac{1}{\tau_N - \tau_0} \int_{\tau_0}^{\tau_N} [|x| - 1]|v| \, \mathrm{d}\tau. \tag{16}$$

Note that the change of sign in v is accounted for in the integrand.

4.2. Fixed point searches

Fixed points of the maps defined by Eqs. (4) and (12) are sought using a globally convergent Newton iteration method for finding the roots of the system of equations

$$\mathbf{P}^k(\bar{\tau}, \bar{\mathbf{d}}) - \begin{pmatrix} \bar{\tau} + \dfrac{2\pi n}{\omega} \\ \bar{\mathbf{d}} \end{pmatrix} = 0, \tag{17}$$

where $\mathbf{d}$ stands for a vector consisting of displacements and velocities and the bar symbol (-) indicates the fixed point. The term global refers to a method which converges to a solution for almost any starting point. The particular algorithm used here has been adapted from Ref. [18].

4.3. Continuation of fixed points and bifurcation points

A sequential continuation scheme is used to map out branches of fixed point solutions, e.g., Refs. [21,22]. Following this scheme, let α be the control parameter (also called the continuation parameter) and divide the interval of interest into closely spaced grid points $\alpha_0, \alpha_1, \ldots, \alpha_N$. The solution $(\bar{\tau}_j, \bar{\mathbf{d}}_j)$ at α_j is used as a prediction for the next solution $(\bar{\tau}_{j+1}, \bar{\mathbf{d}}_{j+1})$ at α_{j+1}. Note that subscript j is used to index the grid points. The predicted value is then corrected with the Newton scheme presented in Section 4.2. For the calculations presented in this paper, the forcing frequency is used as the control parameter ($\alpha = \omega$). Note that, this does not put any restriction on the methods described, i.e., any property of the problem can be used as control parameter, force amplitude, damping ratio, flexural rigidity, etc.

The sequential continuation scheme will obviously fail at bifurcation points where two or more branches meet, e.g., at symmetry breaking bifurcations. In practice, however, one can choose sufficiently small increments in the control parameter to prevent the fixed point from jumping from one branch to another [23].

Cyclic fold bifurcations present another problem for the sequential continuation scheme because the solution vanishes when the control parameter passes through its critical value. This problem can be avoided by interchanging the control parameter α with one of the state variables in $\bar{\mathbf{d}}$ [21].

5. Results of computations

In this section is presented some results of the computations for the SDHO and the beam oscillators. In all the computations, except for the Moon and Shaw experiment, the structural

data given in Table 1 has been chosen, which are representative for a pressurized water reactor fuel rod with a presupposed gap.

5.1. Simple damped harmonic oscillator

The results of the computations for the SDHO are presented in the form of bifurcation diagrams (Figs. 4–6) and phase portraits.

One starts by searching for fixed points for the first iterated map according to relations (4). The bifurcation diagrams, Figs. 4–6, display the response of the system in terms of the impact velocity v versus forcing frequency ω for $w^2 = 132.7415$, $\zeta = 0.005$ and $\beta = 51.0997$ for the first, second and third sub-harmonics, respectively. The diagrams are obtained by using the method described in Sections 2, 4.2 and 4.3. Note that these figures are cut-outs from the full bifurcation diagrams in order to highlight specific features.

Now, consider the first sub-harmonic of motion with the bifurcation diagram shown in Fig. 4 and phase portraits in Fig. 7. From Fig. 7a one can see that for $\omega > 4.625$, there is a stable periodic

Table 1
Structural properties

Mass per unit length	m	0.663 kg/m
Span length	L	0.64 m
Oscillator stiffness	k_1	939.34 N/m
Damping coefficient	c	0.099667 kg/s
Spring stiffness	k_2	123750 N/m
Amplitude	A	6 N
Gap	X_0	1.25×10^{-4} m

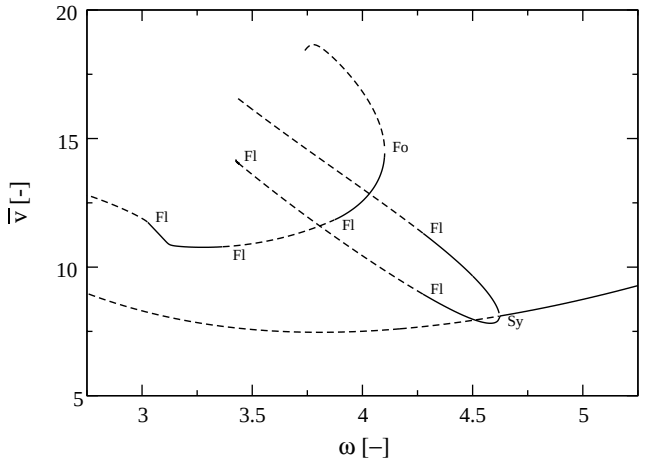

Fig. 4. Period one solutions for the SDHO for the first sub-harmonic ($w^2 = 132.7415$, $\zeta = 0.0050$ and $\beta = 51.0997$), solid and broken lines denote stable and unstable solutions, respectively. Bifurcation points are denoted as Fl = flip, Fo = cyclic fold and Sy = symmetry breaking.

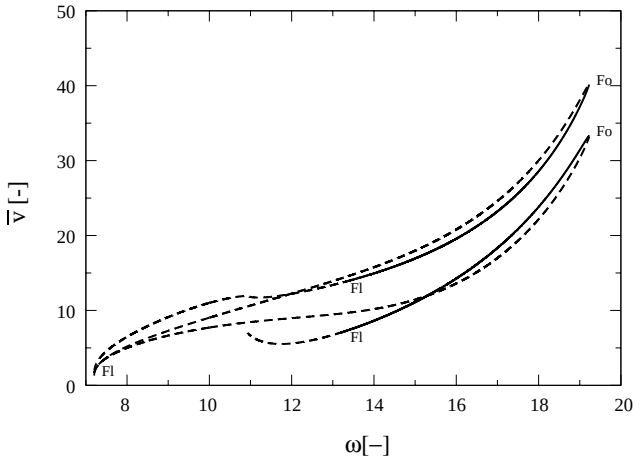

Fig. 5. Period one solutions for the SDHO for the second sub-harmonic ($w^2 = 132.7415$, $\zeta = 0.0050$ and $\beta = 51.0997$), solid and broken lines denote stable and unstable solutions, respectively. Bifurcation points are denoted as Fl = flip and Fo = cyclic fold.

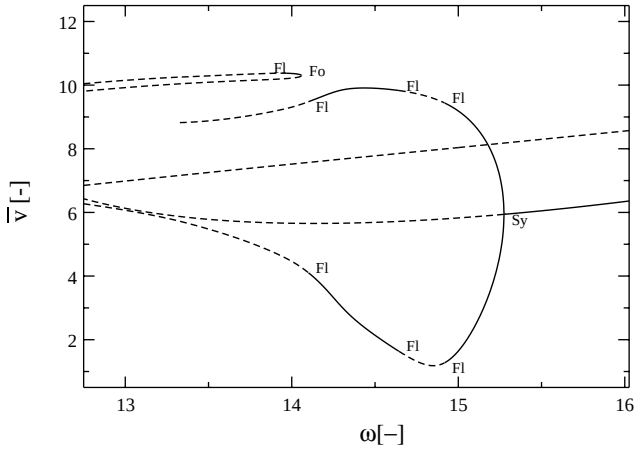

Fig. 6. Period one solutions for the SDHO for the third sub-harmonic ($w^2 = 132.7415$, $\zeta = 0.0050$ and $\beta = 51.0997$), solid and broken lines denote stable and unstable solutions, respectively. Bifurcation points are denoted as Fl = flip, Fo = cyclic fold and Sy = symmetry breaking.

symmetric attractor, since $(\bar{\tau} + \pi n/\omega, -\bar{v})|_{x=-1} = (\bar{\tau}, \bar{v})|_{x=+1}$. This branch of stable periodic solutions will remain stable until the bifurcation point $\omega \approx 11.5$ (not shown in figure) at which it coalesces and gets destroyed by a branch of unstable periodic symmetric solutions. This type of bifurcation is called a cyclic-fold or saddle point bifurcation and it is characterised by a Floquet multiplier leaving the unit circle at $+1$ (Appendix C). Increasing ω beyond this point causes the motion to jump to a remote attractor. The position of the bifurcation point corresponds to resonant peak of the zero-gap linear system ($\omega_1 \approx 11.52$). Furthermore, the low level of damping in

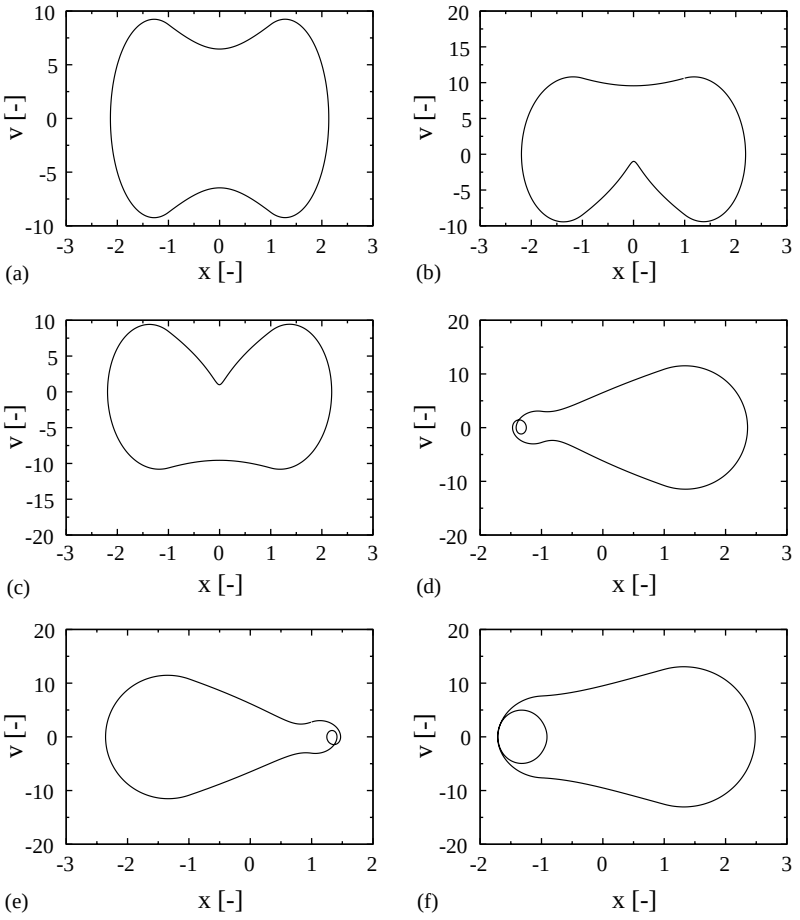

Fig. 7. Phase portraits for the first sub-harmonic of the stable period one solutions for the SDHO. (a) Case 1: $\omega = 5.000$, $\bar{t} \approx -0.176$ and $\bar{v} \approx 8.745$, (b) case 2: $\omega = 4.375$, $\bar{t} \approx -0.258$ and $\bar{v} \approx 10.63$, (c) case 3: $\omega = 4.375$, $\bar{t} \approx -0.0847$ and $\bar{v} \approx 8.469$, (d) case 4: $\omega = 3.125$, $\bar{t} \approx -0.174$ and $\bar{v} \approx 10.88$, (e) case 5: $\omega = 3.125$, $\bar{t} \approx -0.427$ and $\bar{v} \approx 2.764$ and (f) case 6: $\omega = 4.000$, $\bar{t} \approx -0.164$ and $\bar{v} \approx 12.57$.

the system leads to very high velocities close to the bifurcation point $\bar{v} \in [3000, 5000]$, which causes a numerical problem for the present method, since the time spent during the contact phase gets much longer than the time spent during free flight and consequently the algorithm fails to bracket the subsequent root, cf., Section 2.4.

At $\omega = [4.621, 4.622]$ the motion undergoes a supercritical symmetry breaking bifurcation, giving birth to two branches of stable antisymmetric periodic solutions (cf., Figs. 7b and c). This is associated with a Floquet multiplier leaving the unit circle at $+1$ (Appendix C). These two branches are eventually destroyed in period doubling bifurcations at $\omega \in [4.270, 4.275]$, where they continue as unstable branches of periodic solutions. This type of bifurcation is related to a Floquet multiplier leaving the unit circle at -1.

For lower $\omega < 4.11$, one finds stable and unstable asymmetric periodic solutions, e.g., Fig. 7d. Note that each asymmetric solution has a antisymmetric counterpart due to the geometric symmetry of the system, e.g., for the solution shown in Fig. 7d ($\omega = 3.125, \bar{v} = 10.877$), there exists an antisymmetric stable solution for $\omega = 3.125, \bar{v} = 2.7639$, Fig. 7e.

In the interval $\omega \in [3.975, 4.105]$ periodic solutions appear, e.g., Fig. 7f, whose antisymmetric counterpart is no longer a fixed point to the first iterated map. Instead, it appears as a fixed point to the second iterated map for the first sub-harmonic. Table 2 is a compilation of data for the foregoing cases, shown in Fig. 7, concerning stable solutions for the first sub-harmonic of the one iterated map.

Due to the geometric symmetry of the system, symmetric periodic solutions cannot exist for the second sub-harmonic. However, both stable and unstable antisymmetric solutions do exist. Also, due to geometric symmetry, the antisymmetric solution must come in pairs, hence resulting in the double solution branches shown in Fig. 5.

The results for the third sub-harmonic show similar features as for the first sub-harmonic. However, the fixed points for the third sub-harmonic are shifted to higher frequencies and span a narrower range of velocity. This complies with the analytical results of Shaw [6] for an SDHO with rigid amplitude constraints. In Fig. 6, one observes a branch of stable symmetric solutions undergoing a supercritical symmetry breaking bifurcation at $\omega \approx 15.275$, giving birth to two branches of stable antisymmetric fixed solutions, which are then destroyed in flip bifurcations as the forcing frequency is lowered.

Table 2
SDHO test cases

Test case	1	2	3	4
ω	5.000	4.375	4.375	3.125
$\bar{t}$	−0.17555	−0.25785	-8.2160×10^{-2}	−0.17446
$\bar{v}$	8.7454	10.629	8.4687	10.877
Total average work-rate	2.0510	1.9780	1.9780	1.0830
Right[a] average work-rate	1.0255	0.9884	0.9896	0.9176
Left[b] average work-rate	1.0255	0.9896	0.9884	0.1654
Max displacement amplitude	2.1354	2.1922	2.1922	2.3584
Max velocity amplitude	9.2400	10.809	10.809	11.521

Test case	5	6
ω	3.125	4.000
$\bar{t}$	−0.42697	−0.16374
$\bar{v}$	2.7639	12.566
Total average work-rate	1.0830	2.0475
Right[a] average work-rate	0.1654	1.4005
Left[b] average work-rate	0.9176	0.6470
Max displacement amplitude	2.3584	2.4834
Max velocity amplitude	11.521	13.055

[a] Right contact spring at $x = +1$.
[b] Left contact spring at $x = -1$.

5.1.1. Impact work-rate of the SDHO

The impact work-rate has been calculated for the considered SDHO. The results for work rate versus frequency along the stable branches, shown in Fig. 4, are depicted in Fig. 8. The dependence of work-rate on the impact velocity is clearly visible.

For the stable branch of symmetric points $\omega \in [4.622, 11.000]$, one can that the work-rate increases rapidly as the forcing frequency approaches the resonance frequency. The work-rate of the two stable branches ($\omega \in [4.275, 4.621]$) created in the symmetry breaking bifurcation does not branch at the bifurcation point. This is exemplified with cases 2 and 3 listed in Table 2. Instead, the bifurcation manifests itself as a discontinuity.

At the asymmetric periodic solutions, $\omega \in [3.026, 3.364]$, $\omega \in [3.874, 4.100]$, there are significant differences in work-rate between the right and left contact sites (at $x = +1$ and -1, respectively), e.g., cases 4–6 in Table 2 and Figs. 7d–f. Hence, a symmetric impact oscillator described by Eq. (1) may give asymmetric wear damage depending on its initial conditions.

5.2. Beam oscillators

Here, the computations concerning the beam oscillators presented in Section 3 are given. Sections 5.2.1 and 5.2.2 serve as validation of the numerical method described in Section 3. Section 5.2.3 deals with the beam oscillator, representing a vibrating fuel rod, presented in Section 3.1.3.

5.2.1. Beam representation of SDHO

In this section, the methods for finding periodic solutions and computing work-rate in an FE framework, described in Section 3, are validated with a beam representation of the SDHO. The point mass in Fig. 1 is replaced with a beam of unit length and unit radius and high flexural rigidity ($D = 10^5$ N m^2). The beam is modelled by two elements, whose rotational d.o.f.s have been locked. All other properties are set according to the data listed in Table 1.

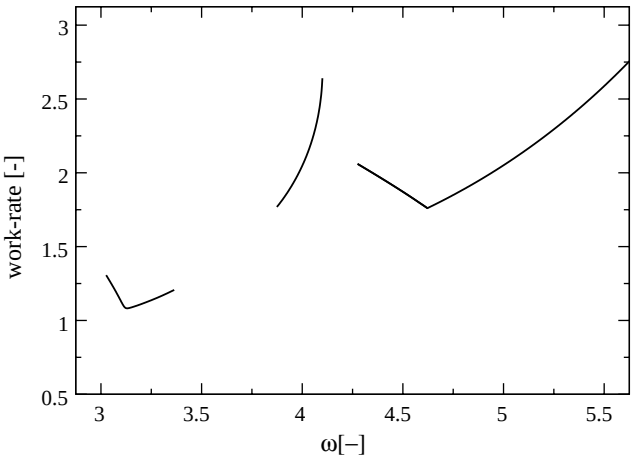

Fig. 8. Impact work-rate along stable branches of the bifurcation diagram for the SDHO as depicted in Fig. 4.

The six test cases listed in Table 2 are re-calculated using the two-element beam oscillator, and comparable results are displayed in Table 3 and Fig. 9. Note that all values given in Table 3 have been rounded off to five significant figures.

The data presented in Tables 2 and 3, and in Figs. 7 and 9 agree well. Typically, the values differ in the third or fourth significant figure. This deviation is due to the fact that the beam is not infinitely stiff.

5.2.2. *Moon and Shaw experiment [12]*

In this section, the computational results for an experiment conducted by Moon and Shaw [12] are given. The results are presented as phase portraits and bifurcation diagrams, in terms of velocity v versus forcing amplitude $a_0 = A_0/\Delta$, where a_0 and A_0 are the non-dimensional and dimensional forcing amplitudes, respectively, and Δ is the one-sided gap in the experiment. The computations have been limited to a forcing frequency of $\Omega = 10.5$ Hz.

The experimental set-up is depicted in Fig. 2. The beam is modelled as a cantilever beam and is excited by a distributed load. In order to simulate the experiment, one is forced to make some assumptions regarding the structural properties. The flexural rigidity $D = EI$ (where E is Young's modulus and I is the moment of inertia of the cross-section of the beam with respect to the neutral axis) was adjusted by matching the three lowest natural frequencies to those reported (4.3, 26 and 73 Hz). Proportional damping is utilized. The structural properties used in the calculations are

Table 3
Test cases with beam representation of SDHO

Test case	1	2	3	4
ω	5.000	4.375	4.375	3.125
$\bar{t}$	−0.17547	−0.25746	-8.2462×10^{-2}	−0.17779
$\bar{v}_c$	8.7692	10.627	8.4897	10.942
Total average work-rate	2.0497	1.9727	1.9727	1.0934
Right[a] average work-rate	1.0249	0.98514	0.98753	0.91802
Left[b] average work-rate	1.0249	0.98753	0.98514	0.17542
Max displacement amplitude	2.1349	2.1909	2.1909	2.3586
Max velocity amplitude	9.2506	10.795	10.795	11.558

Test case	5	6
ω	3.125	4.000
$\bar{t}$	−0.41419	−0.16287
$\bar{v}_c$	2.7681	12.605
Total average work-rate	1.0934	2.0501
Right[a] average work-rate	0.17541	1.4016
Left[b] average work-rate	0.91803	0.64850
Max displacement amplitude	2.3586	2.4838
Max velocity amplitude	11.558	13.065

The displayed data are taken from the node at the contact sites.

[a] Right contact spring at $x = +1$.

[b] Left contact spring at $x = -1$.

compiled in Table 4. The aluminium stop is simulated by a spring with a stiffness based on Young's modulus of aluminium.

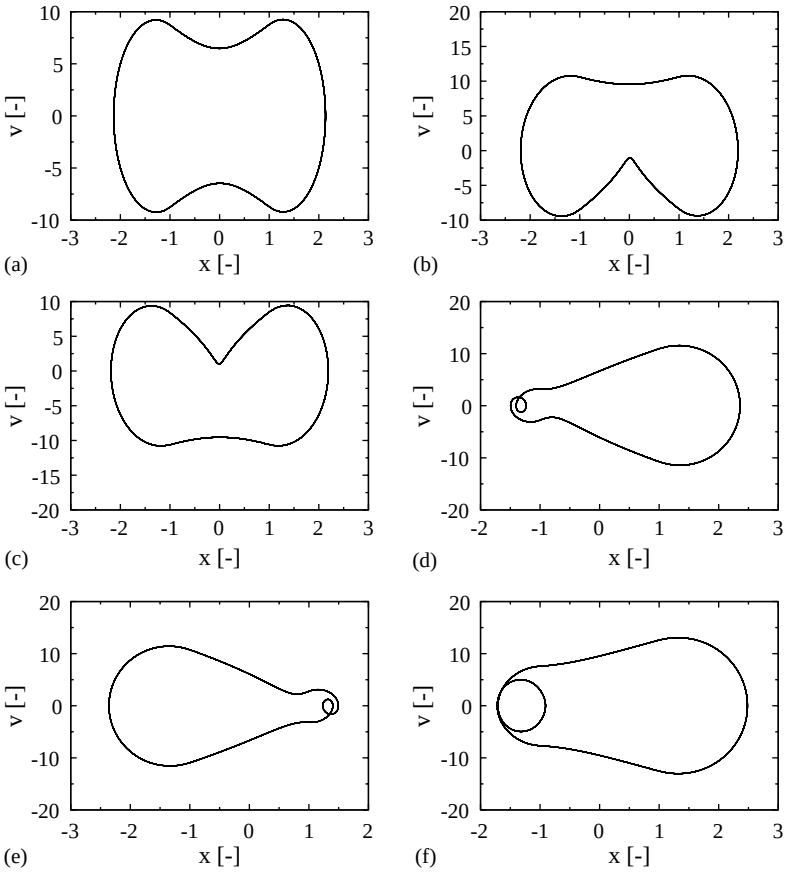

Fig. 9. Phase portraits for the first sub-harmonic of the stable period one solutions for the beam representation of the SDHO, cf., with Fig. 7. The displayed data are taken from the node at the contact sites. (a) Case 1, (b) case 2, (c) case 3, (d) case 4, (e) case 5 and (f) case 6.

Table 4
Structural properties for the Moon and Shaw experiment

Thickness	T	m	0.23×10^{-3}
Width	B	m	9.5×10^{-3}
Length	L	m	0.188
Density	ρ	kg/m^3	7850
Flexural rigidity	D	Nm^2	0.00126533
Mass-proportional damping	c_m	s^{-1}	0.5752
Stiffness-proportional damping	c_k	s	5.024×10^{-4}
Impact spring stiffness	k_{Al}	N/m	6.65×10^{8}
One-sided gap	Δ	m	3×10^{-3}

This selection of material properties gives rise to considerable numerical chattering at the structural interface, which propagates to uncertainty in Jacobian evaluation and poor convergence in the fixed point iteration. The solution is twofold (i), reduce the time step and (ii) choose another Poincaré section.

As pointed out by Johansson [16], reducing the time step reveals the finer structure of the contact force variation while the global motion changes only slightly. Consequently, the time step is set short enough to accurately predict motion away from the structural interface and define the Poincaré section, Σ, in this region of phase space. This is indicated in Fig. 10a, which shows a stable one periodic attractor for the first sub-harmonic.

Fig. 10b shows a stable period two attractor, which is born in a flip bifurcation at $a_0 \approx 0.47$, from a period one second sub-harmonic solution. This is shown in the bifurcation diagram (Fig. 11). This complies with the experimental findings by Moon and Shaw [12]. However, no period doubling cascade was found in the numerical simulations. Instead, one finds reformation

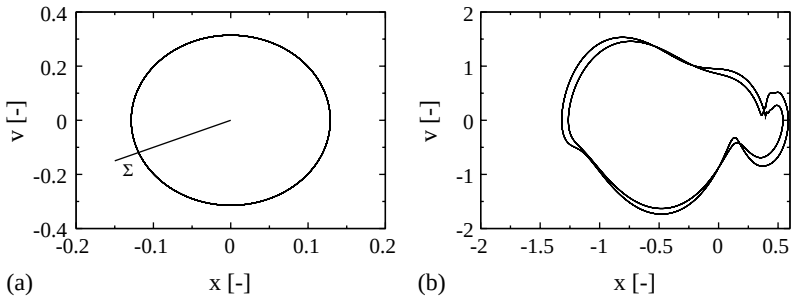

Fig. 10. Phase portraits for the Moon and Shaw experiment for $\Omega = 10.5$ Hz. Σ denotes the chosen Poincaré section. Displayed data are from the structural properties according to Table 4. (a) For forcing amplitude, $A_0 = 0.7 \times 10^{-3}$ (m), first sub-harmonic, stable periodic attractor. (b) $A_0 = 1.5 \times 10^{-3}$ [m], period doubled attractor.

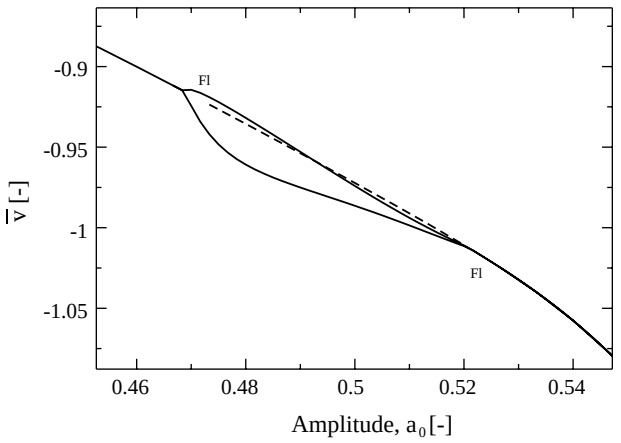

Fig. 11. Fixed point solutions for the Moon and Shaw experiment [12] ($\Omega = 10.5$ Hz). Solid and broken lines denote stable and unstable solutions, respectively.

of a stable period one second sub-harmonic attractor through flip bifurcation as the amplitude is increased. Consequently, no chaotic solutions were found in the simulations.

5.2.3. Fuel rod oscillator

This section comprises the results of computations made for the beam oscillator (Fig. 3) representing a portion of a vibrating fuel rod. In Ref. [10], stable periodic cycles were identified for $\omega \in [5, 6.5]$ and $\omega \in [9, 10]$ by performing extensive time integrations. Here, the Poincaré map method is used to directly determine the stable periodic solutions. From these fixed points, one can then follow the solution branches by sequential continuation, according to the methods described in Sections 3 and 4.3, to produce a bifurcation diagram in the form of frequency–response curves as presented for the SDHO in Section 5.1. Furthermore, phase portraits are presented to highlight some features of the dynamics. Note that the dynamics of the beam oscillator is represented by the motion at the contact node throughout this section.

The structural properties specific to the fuel rod oscillator are given in Table 5, [10]. Other properties are set according to data in Table 1.

Figs. 12a and b show phase portraits at the contact node for $\omega = 5.1$ and 9.6, respectively, and display two stable symmetric solutions, i.e., $(\bar{\tau} + \pi n/\omega, -\bar{\mathbf{x}}^r, -\bar{\mathbf{v}})|_{x=-1} = (\bar{\tau}, \bar{\mathbf{x}}^r, \bar{\mathbf{v}})|_{x=+1}$. The phase portraits were generated by initiating the time integration from the fixed point and continuing it over 100 forcing cycles, of which approximately the last 10 cycles are shown in the figures.

Table 5
Properties specific for the beam oscillator with fuel rod dimensions

Beam density	ρ	kg/m^3	9347.51
Cross-section area	$\mathscr{A}$	m^2	7.088×10^{-5}
Beam length	L	m	0.64
Mass-proportional damping	c_m	s^{-1}	0.3984
Stiffness-proportional damping	c_k	s	2.975×10^{-5}
Flexural rigidity	D	Nm^2	24.90
Lateral support spring stiffness	k_{tra}	N/m	1.48×10^5
Torsion support spring stiffness	k_{rot}	N/m	5.35×10^2
Contact spring stiffness	k_c	N/m	123750

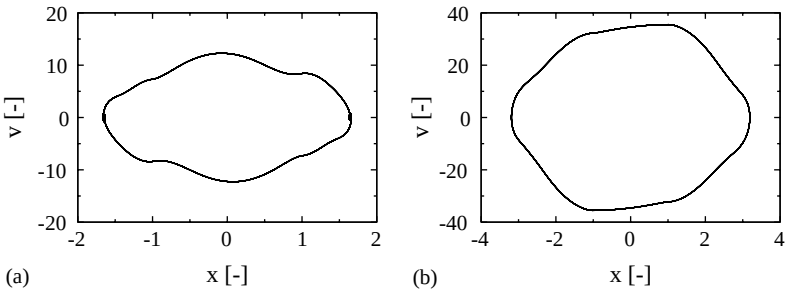

Fig. 12. Phase portraits for the first sub-harmonic of the stable period one solutions for the beam oscillator. The displayed data are taken from the node at the contact sites: (a) example 3: $\omega = 5.1$ and (b) example 8: $\omega = 9.6$.

By computing the continuation from the periodic fixed points, displayed in Fig. 12, one finds stable and unstable branches of period one solutions. These are displayed in Fig. 13. As expected, the branches follow more complex paths compared to the SDHO (Section 5.1). However, similar features are not hard to find.

Below $\omega = 5$, almost no stable period one solutions are found. This behaviour is in line with previously published results [10]. However, two short intervals with stable solutions are identified, $\omega \in [3.575, 3.582]$ and $\omega \in [3.643, 3.664]$. Figs. 14a and b show examples of phase portraits taken from respective regions (Example 1: $\omega = 3.58$ and Example 2: $\omega = 3.65$). These orbits are clearly asymmetric; however, they have antisymmetric counterparts for the first sub-harmonic of the second iterated map.

Above $\omega = 5$ stable solutions become more frequent. First, one finds a region of stable symmetric orbits in the interval $\omega \in [5.02, 5.28]$ (e.g., Example 3: $\omega = 5.1$ in Fig. 12a).

Similar to the SDHO system in Section 5.1, one can identify a supercritical symmetry breaking bifurcation. Here, there is a bifurcation in the vicinity of $\omega = 5.629$, which is

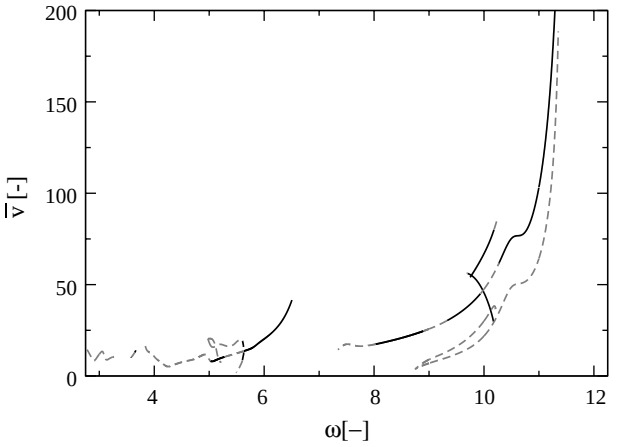

Fig. 13. Stable (solid lines) and unstable (broken lines) period one solutions for the first sub-harmonic of the fuel rod oscillator. The displayed data are taken from the node at the contact sites.

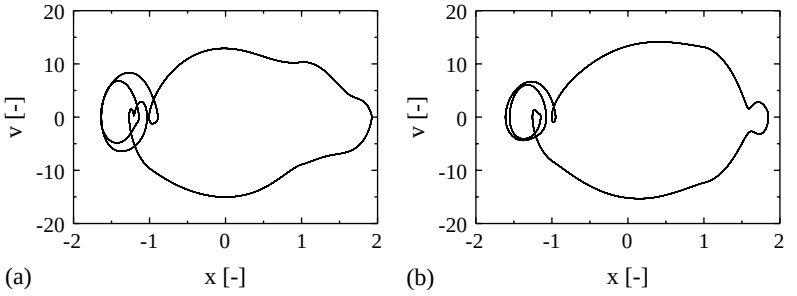

Fig. 14. Phase portraits for the stable periodic solutions for the first sub-harmonic at low forcing frequencies applied to the fuel rod oscillator: (a) example 1: $\omega = 3.58$ and (b) example 2: $\omega = 3.65$.

somewhat higher than that for the SDHO. Phase-plane orbits are shown just before (Example 4: $\omega = 5.70$ in Fig. 15a) and just after (Examples 5 and 6: $\omega = 5.61$ in Figs. 15b and c, respectively) the bifurcation point. The stable branches of antisymmetric solutions created are quickly destroyed in what appears to be secondary Hopf or Neimark bifurcations, i.e., when two complex conjugate Floquet multipliers leave the unit circle away from the real axis. Beyond $\omega = 6.506$ it was impossible to follow the stable branch of symmetric solutions, that is the solution switches from being a period one point to a period two point on the Poincaré map without bifurcating. This discontinuity in the Poincaré map is associated with $\bar{v} = 0$ at $x_c = +1$.

At $\omega = 7.343$ a branch of symmetric period one solutions appears. The first region of stable solutions is found in the interval $\omega \in [8.04, 8.90]$. The interval is started and ended by Neimark bifurcations. The phase portrait in Fig. 16a shows an orbit for $\omega = 8.50$ (Example 7). The second and third stable regions along the symmetric branch are found in intervals $\omega \in [9.33, 9.93]$ and $[10.28, 11.35]$, respectively. Phase portraits from these regions are shown in Figs. 12b (Example 8: $\omega = 9.60$) and 16b (Example 9: $\omega = 11.0$), respectively.

The last two branches of stable period one orbits, identified in the fixed point search (Fig. 13), are found to lie in the frequency intervals $\omega \in [9.75, 10.18]$ and $\omega \in [9.71, 10.17]$. They consist of corresponding antisymmetric orbits. This is exemplified in Figs. 17a and b (Examples 10 and 11: $\omega = 9.9$).

Data for the examples, discussed above and shown in Figs. 12 and 14–17, are listed in Table 6.

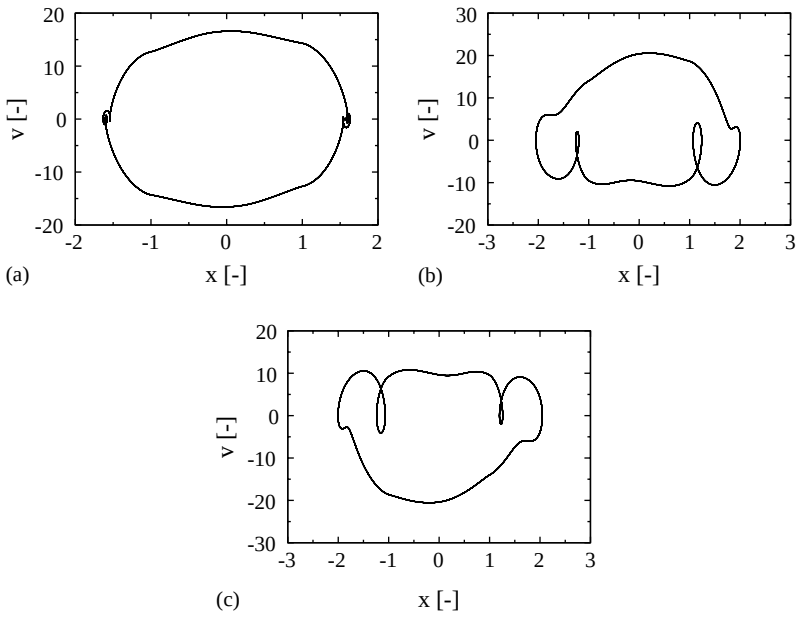

Fig. 15. Phase portraits of the stable period one solutions close to the supercritical symmetry breaking bifurcation for the first sub-harmonic of the fuel rod oscillator. The displayed data are taken from the node at the contact sites: (a) example 4: $\omega = 5.70$, (b) example 5: $\omega = 5.61$ and (c) example 6: $\omega = 5.61$.

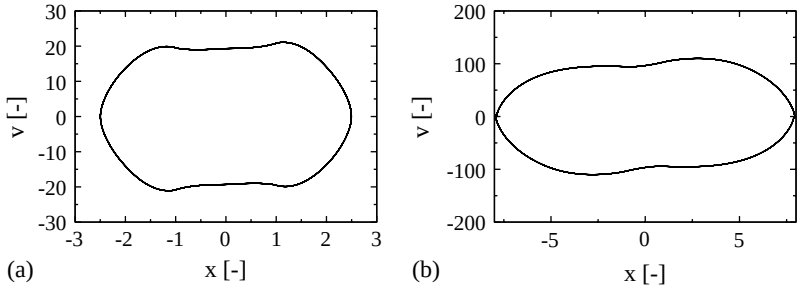

Fig. 16. Phase portraits for the stable period one solutions along symmetric branch for the first sub-harmonic of the fuel rod oscillator. The displayed data are taken from the node at the contact sites: (a) example 7: $\omega = 8.50$ and (b) example 9: $\omega = 11.0$.

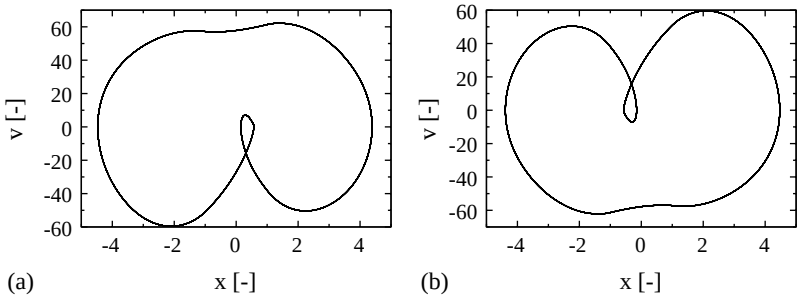

Fig. 17. Phase portraits for the stable asymmetric period one solutions for the first sub-harmonic of the fuel rod oscillator. The displayed data are taken from the node at the contact sites: (a) example 10: $\omega = 9.90$ and (b) example 11: $\omega = 9.90$.

5.2.4. *Impact work-rate of the fuel rod oscillator*

Here the results from the work-rate calculations for the fuel rod oscillator considered in Section 5.2.3 are presented. The impact work-rate was calculated according to the method described in Section 4.1 along the stable branches shown in Fig. 13.

Figs. 18a and b show the impact work-rate evaluated at fixed points along the stable branches for $\omega < 7.0$ and $\omega > 7.0$, respectively. Similar to the SDHO in Section 5.1, one notes the overall dependence of work-rate on the impact velocity, i.e., higher impact velocity gives higher work-rate. However, this is not always the case, e.g., compare Fig. 13 with Figs. 18a and b. After the symmetry breaking bifurcation at $\omega \approx 6.629$, two branches of antisymmetric stable solutions are created when the forcing frequency ω is lowered below the bifurcation point, one with increasing impact velocity and one with decreasing impact velocity, respectively (Fig. 13). However, in Fig. 18a it can be seen that the two coincident stable branches, created through the bifurcation, are characterized by a sharp increase in work rate. This behaviour is a result of the double-impact motion of the system. Fig. 15b shows the phase portrait of a stable antisymmetric solution after the bifurcation. Note the high impact velocity at $x = +1$ and the much lower impact velocity at $x = -1$. For the corresponding antisymmetric solution shown in Fig. 15c the situation is vice

Table 6
Examples for the fuel rod oscillator

Example	1	2	3	4
ω	3.580	3.650	5.100	5.700
$\bar{t}$	−0.16669	−0.18328	−0.20243	−0.20292
$\bar{v}_c$	10.329	13.148	8.4025	14.309
Total average work-rate	0.97779	0.83658	0.73765	0.78435
Right[a] average work-rate	0.48521	0.41801	0.36882	0.39218
Left[b] average work-rate	0.49258	0.41857	0.36883	0.39218
Max displacement amplitude	1.9228	1.8483	1.6608	1.6334
Max velocity amplitude	15.034	15.321	12.277	16.599
Example	5	6	7	8
ω	5.610	5.610	8.500	9.600
$\bar{t}$	−0.21847	−0.16549	−0.12967	−0.12668
$\bar{v}_c$	18.629	9.5478	20.817	35.526
Total average work-rate	1.9514	1.9514	6.0622	14.645
Right[a] average work-rate	0.94702	1.0044	3.0311	7.3226
Left[b] average work-rate	1.0043	0.94705	3.0311	7.3229
Max displacement amplitude	2.0472	2.0468	2.4969	3.1893
Max velocity amplitude	20.556	20.553	21.082	35.527
Example	9	10	11	
ω	11.00	9.900	9.900	
$\bar{t}$	−0.096098	−0.10420	−0.63197	
$\bar{v}_c$	103.34	61.365	50.941	
Total average work-rate	168.07	37.074	37.074	
Right[a] average work-rate	84.034	18.092	18.982	
Left[b] average work-rate	84.034	18.982	18.092	
Max displacement amplitude	7.9277	4.4709	4.4710	
Max velocity amplitude	110.01	62.170	62.172	

The listed data are taken from the node at the contact sites.
[a] Right contact spring at $x = +1$.
[b] Left contact spring at $x = -1$.

versa. However, since the work-rate is evaluated over the entire orbit, the two solutions have the same work-rate. This also applies for the two stable branches of antisymmetric solutions found in the forcing frequency interval $\omega \in [9.75, 10.17]$; compare Fig. 13 with Fig. 18b (cf., also Figs. 17a and b).

Another general observation is that stable asymmetric orbits render higher average work-rate than the symmetric orbits at or close to the same forcing frequency. This can be seen both in Fig. 18a, where a sharp increase in work-rate is visible as the forcing frequency is lowered below the symmetry breaking bifurcation at $\omega \approx 5.629$ (cf., also Examples 4–6 in Table 6) and in Fig. 18b, where the line corresponding to the work-rate at the two stable branches of mutually antisymmetric orbits lie well above the lines showing the work-rate at stable symmetric orbits (cf., Examples 8, 10 and 11 in Table 6).

In the interval $\omega \in [5.018, 5.284]$, one also observes an increasing work-rate for decreasing ω. This seems to be connected to the development of loops in the phase-plane, which is shown in the portraits in Fig. 19. The loop formation is accompanied by an increasing peak contact force.

Comparing the results of the SDHO and the fuel rod oscillator, one can see that the difference in the work-rate between the left and right contact sites for an asymmetric orbit is far less for the fuel rod oscillator than for the SDHO. Despite this the SDHO used here is regarded as a one-dimensional representation of the fuel rod oscillator. Thus, indicating that one can study some aspects of the fuel rod vibro-impact dynamics using an SDHO simplification.

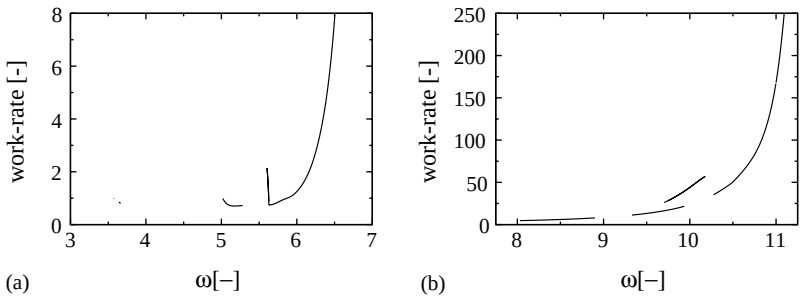

Fig. 18. Impact work-rate for the fuel rod oscillator evaluated along the stable branches shown in Fig. 13 for (a) $\omega < 7.0$ and (b) $\omega > 7.0$, respectively.

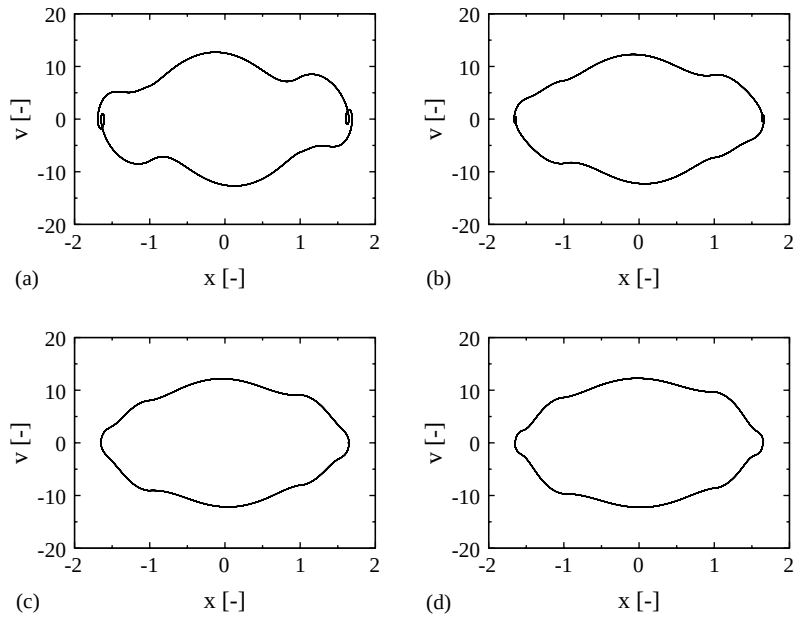

Fig. 19. Phase portraits for the fuel rod oscillator at (a) $\omega = 5.05$, (b) $\omega = 5.10$, (c) $\omega = 5.15$ and (d) $\omega = 20$, respectively.

6. Conclusion

The dynamics of interaction of four different impact oscillators subject to harmonic excitation has been analyzed. More specifically, the existence and stability of periodic orbits and the local bifurcation thereof are numerically evaluated. Impact work-rate, which is the rate of energy dissipated to the impacting surfaces, is evaluated. This property is a measure of the available energy for surface damage and is calculated along stable branches of period one orbits.

Firstly, the dynamics of an impact oscillator in its simplest form, i.e., a mass, spring, damper system with two-sided elastic amplitude constraints (SDHO) was studied. The system was assigned properties relevant to a vibrating nuclear fuel rod. The resulting dynamics is well in line with what has been found for an oscillator with rigid amplitude constraints [6]. However, in the analysis, asymmetric orbits have also been included. It has been shown that asymmetric orbits render asymmetric work-rates on the symmetrically placed constraints. Furthermore, these orbits have higher work-rates than symmetric orbits at or near the same forcing frequency. From Ref. [10] one learns that aperiodic or chaotic solutions do exist for lower forcing frequencies. The current analysis shows that the route to chaos is initiated with a supercritical symmetry breaking bifurcation followed by a sequence of flip bifurcations. This is also in agreement with results for oscillators with rigid constraints (cf., Ref. [24]).

Secondly, to validate the numerical methods, the simplest two-sided impact oscillator was re-modelled using a cylindrical beam with unit length and radius. To enable direct comparison with the SDHO, the beam is given an artificial flexural rigidity and all the rotational degrees of freedom are locked down. The numerical method used to find periodic orbits of the vibrating beam converged to practically the same values as found for the SDHO. Furthermore, phase portraits for the two systems were virtually identical and work-rates were found to have negligible deviation.

Thirdly, attention was turned towards an experiment conducted by Moon and Shaw [12]. To analyze the experiment, some assumptions regarding the structural properties of the cantilevered beam were made. The flexural rigidity of the beam was set by matching the first three natural eigenfrequencies to measurements. The associated Young's modulus, E, was checked against tabulated data for steel and found to be reasonable. In the experiment, constrained layer damping was added by taping a shim steel on both sides of the beam. In the evaluation, the Rayleigh damping coefficients were set to give correct damping at the first eigenfrequency. Computations for a forcing frequency of 10.5 Hz could reproduce the bifurcation from a stable period one sub-harmonic two-orbit solution to a period two sub-harmonic four-orbit solution. Other forcing frequencies were explored and longer period-doubling cascades were identified. However, a chaotic attractor could not be found. Two sources of the discrepancy between reality and simulation can immediately be identified: (i) load application and (ii) Rayleigh damping. For the applied load, a distributed load was used rather than a displacement load as employed in the experiment. With regard to damping, the stiffness-proportional part of the Rayleigh damping will supply higher damping at higher frequencies. This feature, although attractive numerically, is not necessarily a correct one. To further evaluate the results of the Moon and Shaw experiment these issues need to be resolved.

Finally, the methodology has been applied to a two-dimensional representation of a vibrating fuel rod. For lower frequencies the beam shows similar dynamic response compared to the

SDHO, i.e., similar phenomena are found in both cases. However, the similarities must not be exaggerated. Impact velocities and work-rates are of the same magnitude as the corresponding values for the SDHO, whereas phase portraits of orbits are more "wrinkled" and the patterns of stable and unstable branches are more complex in the fuel rod oscillator. The results for the SDHO showed significant differences in work-rate between the symmetric constraints, i.e., between the right and the left contact sites. For the fuel rod oscillator, this difference is there, but it is not as pronounced. Moreover, work-rate for asymmetric orbits is significantly higher than for symmetric orbits at or near the same frequency, as predicted using the SDHO.

Wear is a slow process in any well-designed engineering system. Further, harmonic excitation is a feature of many of these systems (e.g., turbines). Hence, the study of periodic orbits in a harmonically vibrating system with wear is relevant. Note that systems with combined loading (harmonic and stochastic) can also behave as periodic attractors, see e.g., Ref. [25]. The method described in this paper can be used to assess the wear susceptibility of beam-like structures that are subject to impact vibrations.

Acknowledgements

The work was supported by the Swedish Foundation for Knowledge and Competence Development (KKS) under Award HÖG 212/01.

Appendix A. Solution to the simple damped harmonic oscillator

For the sake of completeness, the analytic solution of the simple damped harmonic oscillator with symmetric elastic constraints presented in Section 2, Eq. (1) is included. This solution originates from Ref. [5], which has been adapted to include double-impact motion [10] and here time reversal property. It is written as

$$x(\tau) = x_{tr}(\tau) + x_{st}(\tau) + \operatorname{sgn}(\tau)\operatorname{sgn}(v_i)(1/w_i^2 - 1); \quad i = \{0, 1, \ldots, N\} \tag{A.1}$$

with

$$x_{tr}(\tau) = \mathrm{e}^{-\zeta(\tau-\tau_i)}\{A_i \cos[\Omega_i(\tau-\tau_i)] + B_i \sin[\Omega_i(\tau-\tau_i)]\},$$

$$x_{st}(\tau) = \gamma_i \cos(\omega\tau) + \delta_i \sin(\omega\tau),$$

$$A_i = -\gamma_i c_i - \delta_i s_i + (-1)^i \operatorname{sgn}(\tau)\operatorname{sgn}(v_i)/w_i^2,$$

$$B_i = [v_i + (-1)^i \operatorname{sgn}(\tau)\operatorname{sgn}(v_i)\zeta/w_i^2 + s_i(\gamma_i\omega - \delta_i\zeta) - c_i(\gamma_i\zeta + \delta_i\omega)]/\Omega_i,$$

$$\gamma_i = (w_i^2 - \omega^2)\beta/\Delta_i,$$

$$\delta_i = 2\zeta\omega\beta/\Delta_i,$$

$$\Delta_i = (w_i^2 - \omega^2)^2 + (2\zeta\omega)^2,$$

$$\Omega_i^2 = w_i^2 - \zeta^2,$$

$$c_i = \cos(\omega\tau),$$

$$s_i = \sin(\omega\tau), \tag{A.2}$$

where even and odd i yield motion during contact and free flight, respectively, and $\mathrm{sgn}(\tau)$ defines the direction of the time flow.

Appendix B. Evaluation of Jacobian

The Jacobian for the SDHO system with symmetric elastic constraints is

$$\left[\frac{\partial(\tau_{i+1}, v_{i+1})}{\partial(\tau_i, v_i)}\right] = \begin{bmatrix} \dfrac{\partial\tau_{i+1}}{\partial\tau_i} & \dfrac{\partial\tau_{i+1}}{\partial v_i} \\ \dfrac{\partial v_{i+1}}{\partial\tau_i} & \dfrac{\partial v_{i+1}}{\partial v_i} \end{bmatrix}, \tag{B.1}$$

where

$$\frac{\partial\tau_{i+1}}{\partial\tau_i} = \frac{\mathrm{e}^{-\zeta(\tau_{i+1}-\tau_i)}}{v_{i+1}}\left\{ v_i \cos[\Omega_i(\tau_{i+1}-\tau_i)] - \frac{1}{\Omega_i}[\zeta v_i + (-1)^i \,\mathrm{sgn}(v_i) - \beta\cos(\omega\tau_i)]\sin[\Omega_i(\tau_{i+1}-\tau_i)]\right\}, \tag{B.2}$$

$$\frac{\partial\tau_{i+1}}{\partial v_i} = \frac{-\mathrm{e}^{-\zeta(\tau_{i+1}-\tau_i)}\sin[\Omega_i(\tau_{i+1}-\tau_i)]}{v_{i+1}\Omega_i}, \tag{B.3}$$

$$\frac{\partial v_{i+1}}{\partial\tau_i} = \frac{\partial\tau_{i+1}}{\partial\tau_i}a_{i+1} + \mathrm{e}^{-\zeta(\tau_{i+1}-\tau_i)}\left\{[2\zeta v_i + (-1)^i\,\mathrm{sgn}(v_i) - \beta\cos(\omega\tau_i)]\cos[\Omega_i(\tau_{i+1}-\tau_i)] + \left[v_i\frac{\Omega_i^2-\zeta^2}{\Omega_i} + \frac{\zeta}{\Omega_i}\{-(-1)^i\,\mathrm{sgn}(v_i) + \beta\cos(\omega\tau_i)\}\right]\sin[\Omega_i(\tau_{i+1}-\tau_i)]\right\}, \tag{B.4}$$

$$\frac{\partial v_{i+1}}{\partial v_i} = \frac{\partial\tau_{i+1}}{\partial v_i}a_{i+1} + \mathrm{e}^{-\zeta(\tau_{i+1}-\tau_i)}\left\{\cos[\Omega_i(\tau_{i+1}-\tau_i)] - \frac{\zeta}{\Omega_i}\sin[\Omega_i(\tau_{i+1}-\tau_i)]\right\}. \tag{B.5}$$

Appendix C. Bifurcations of periodic orbits

Periodic motion of a constrained oscillating system can be studied by a Poincaré map P, see for example Ref. [26]. Each iteration of P corresponds to a contact of mass m with the constraints at $x = \pm 1$ and relates the time and velocity at the previous encounter to those of the subsequent one. A motion that repeats after k contacts must satisfy the following condition:

$$\left(\bar{\tau} + \frac{2\pi n}{\omega}, \bar{v}\right) = P^k(\bar{\tau}, \bar{v}), \tag{C.1}$$

where P^k denotes that P has been applied k times. According to condition (C.1), the motion repeats itself after k encounters with the Poincaré section at $x = \pm 1$ after n cycles. Such a motion is referred to as a *sub-harmonic* of order n. The point $(\bar{\tau}, \bar{v})$ is called a *periodic point* of P.

The stability of periodic motion can be investigated by examining whether the motion near the periodic motion is attracted towards or repelled from the periodic solution. A small disturbance in proximity of $(\bar{\tau}, \bar{v})$ allows us to express condition (C.1), after expansion in Taylor series and linearizing, in the manner

$$(\zeta_{j+1}, \eta_{j+1}) = \bar{\mathscr{D}} P^k(\zeta_j, \eta_j), \tag{C.2}$$

where (ζ, η) is the disturbance around $(\bar{\tau}, \bar{v})$ and $\bar{\mathscr{D}} P^k$ is the first derivative (Jacobian matrix of $2k$-dimension) of P^k evaluated at the periodic point. Note that the stability analysis is local since the disturbance is localized.

The stability criterion is established in terms of the eigenvalues λ_j of the Jacobian matrix $\bar{\mathscr{D}} P^k$. For the linear system (C.2), the periodic orbit is asymptotically stable if and only if the spectrum of $\bar{\mathscr{D}} P^k$ lies within a unit circle in the complex λ plane, i.e., $|\lambda_j| < 1$. When λ_j leaves the unit circle, three situations can be envisaged. (i) An eigenvalue leaves the unit circle through $\lambda_i = +1$, resulting in the following three bifurcations: *transcritical*, *symmetry-breaking*, and *cyclic-fold* bifurcations. (ii) An eigenvalue leaves the unit circle through $\lambda_i = -1$, resulting a *period-doubling* bifurcation. (iii) Two complex conjugate eigenvalues leave the unit circle away from the real axis, resulting a *Hopf* bifurcation.

References

[1] M.J. Pettigrew, C.E. Taylor, N.J. Fisher, M.Yetsir, B.A.W. Smith, Flow-induced vibration: recent findings and open questions, Nuclear Engineering and Design 185 (1998) 249–276.

[2] C.C. Fu, B. Paul, Dynamic stability of a vibrating hammer, Transactions of the American Society of Mechanical Engineers, Journal of Engineering for Industry (November 1969) 1175–1179.

[3] A.F. Vakakis, J.W. Burdick, Chaotic dynamics in the motion of a hopping robot, in: Proceedings of IEEE International Conference on Robotics and Automation, Vol. 110, 1990, pp. 1464–1469.

[4] R. Vilelamendes, M. Defaria, L. Streit, Map dynamics in gear box model, Technical Report BIBOS-250/87; ETN-87-90364, Forschungzentrum Bielefeld-Bochum-Stochastic, Bielefeld, Germany, 1987.

[5] S.W. Shaw, P.J. Holmes, A periodically forced piecewise linear oscillator, Journal of Sound and Vibration 90 (1) (1983) 129–155.

[6] S.W. Shaw, The dynamics of a harmonically excited system having rigid amplitude constraints, Part 1: subharmonic motions and local bifurcations, Journal of Applied Mechanics 52 (1985) 453–458.

[7] J.O. Aidanpää, R.B. Gupta, Periodic and chaotic behaviour of a threshold-limited two-degree-of-freedom system, Journal of Sound and Vibration 165 (1993) 305–327.

[8] D. Pun, S.L. Lau, S.S. Law, D.Q. Cao, Force vibration analysis of a multidegree impact vibrator, Journal of Sound and Vibration 213 (1998) 447–466.

[9] P.L. Ko, Wear of power plant components due to impact and sliding, Applied Mechanics Review 50 (7) (1997) 387–411.

[10] J. Knudsen, A.R. Massih, Vibro-impact dynamics of a periodically forced beam, Journal of Pressure Vessel Technology 122 (2000) 210–221.

[11] J. Knudsen, A.R. Massih, R. Gupta, Analysis of a loosely supported beam under random excitations, in: S. Ziada, T. Staubli (Eds.), Flow-Induced Vibration, Balkema, Roterdam, June 2000, pp. 505–512.

[12] F.C. Moon, S.W. Shaw, Chaotic vibrations of a beam with non-linear boundary conditions, International Journal of Non-linear Mechanics 18 (6) (1983) 465–477.

[13] J. Knudsen, A.R. Massih, L. Johansson, Calculation of vibro-impact dynamics of loosely supported rods, in: Fluid Structure Interaction, Aeroelasticity, Flow Induced Vibration and Noise AD-Vol 53-1, I, ASME, New York, 1997.
[14] J. Knudsen, A.R. Massih, Analysis of a loosely supported beam under harmonic excitation, in: M.P. Pettigrew (Ed.), PVP-Vol. 389, Flow-Induced Vibration—1999, ASME, New York, August 1999, pp. 265–272.
[15] M. Petyt, Introduction to Finite Element Vibration Analysis, Cambridge University Press, Cambridge, 1990 (Chapter 9).
[16] L. Johansson, Beam motion with unilateral contact constraints and wear of contact sites, Journal of Pressure Vessel Technology 119 (1997) 105–110.
[17] N. Strömberg, L. Johansson, A. Klarbring, Derivation and analysis of a generalized standard model for contact, friction and wear, International Journal of Solids and Structures 33 (1996) 1817–1836.
[18] W.H. Press, S.A. Teukolsky, W.T. Vetterling, B.P. Flannery, Numerical Recipes in Fortran90: The Art of Parallel Scientific Computing, 2nd Edition, Cambridge University Press, Cambridge, 1996.
[19] M. Metcalf, J. Reid, FORTRAN 90/95 Explained, 2nd edition, Oxford University Press, Oxford, England, 1999.
[20] T.M. Frick, E. Sobek, J.R. Reavis, Overview on the development and implementation of methodologies to compute vibration and wear of steam generator tubes, in: M.P. Paidoussis, J.M. Chenoweth, M.D. Bernstein (Eds.), ASME Special Publication, Symposium on Flow-Induced Vibrations in Heat Exchangers, New Orleans, Louisiana, December 1984, pp. 149–160.
[21] J. Rinzel, R.N. Miller, Numerical calculation of stable and unstable periodic solutions to the Hodgkin–Huxley equations, Mathematical Biosciences 49 (1980) 27–59.
[22] R. Seydel, Numerical computation of periodic orbits that bifurcate from stationary solutions of ordinary differential equations, Applied Mathematics and Computation 9 (1981) 257–271.
[23] J.G. Byatt-Smith, 2π periodic solutions of Duffing's equation with negative stiffness, SIAM Journal of Applied Mathematics 47 (1) (1987) 60–91.
[24] S.W. Shaw, The dynamics of a harmonically excited system having rigid amplitude constraints, Part 2: chaotic motions and global bifurcations, Journal of Applied Mechanics 52 (1985) 459–464.
[25] D. Roy, Non-chaotic response of non-linear oscillators under combined deterministic and weak stochastic excitations, Journal of Sound and Vibration 225 (4) (1999) 741–766.
[26] J. Guckenheimer, P. Holm, Nonlinear Oscillations, Dynamic Systems, and Bifurcations of Vector Fields, Springer, New York, 1986.